Tribology Letters (2019) 67:8
https://doi.org/10.1007/s11249-018-1124-9

ORIGINAL PAPER

Effects of Normal Load on the Coefficient of Friction by Microscratch Test of Copper with a Spherical Indenter

Chenghui Gao[1] · Ming Liu[1]

Received: 12 September 2018 / Accepted: 25 November 2018 / Published online: 29 November 2018

Abstract
A Rockwell C 120° diamond indenter with a spherical tip radius of 100 µm was used to measure the coefficient of friction by microscratch test under different normal loads. The measured friction coefficient was found to increase with normal load, which was rationalised by a geometrical intersection model. Although plastic deformation increases with normal load, its contribution into the total deformation becomes smaller with the increase in normal load. Elastic deformation predominates in the total deformation under large normal loads. It is the adhesion shear stress over the contact area that causes plastic deformation. Lateral force was found to be proportional to penetration depth, especially under large normal loads when elastic deformation predominated the deformation, with the proportionality representing deformation or shearing resistant toughness.

Keywords Microscratch test · Spherical indenter · The coefficient of friction · Effects of normal load · Scratch-induced deformation

1 Introduction

Scratch test [1], which is especially suitable to study scratch-induced failure of coating by wear debris and particles, has been widely used for material characterisation such as scratch hardness [2], wear and damage [3], fracture toughness [4], strength of material [5], coating failure, scratch behaviour of coating, critical loads [6], adhesion strength [7] and bond strength between film and substrate [8, 9], in order to understand tribological behaviour of material in complex mechanical situations [10] for applications like the design of coatings [11–13], indicators of film adhesion strength [14–16] and simulation of machining [17]. Charitidis et al. [18] investigated nanoscratching behaviour of amorphous carbon films, and correlated abrupt changes of friction coefficients and displacements with fractures such as delamination and cracking. Huang et al. [19] analysed elastic–plastic deformation of diamond-like carbon films on Ti alloy substrate by nanoscratch test, and found elastic deformation predominated in the total deformation before coating failure. Akono et al. [4] proposed a model of scratch test for determining fracture toughness from horizontal force and contact geometry using linear elastic fracture mechanics methods, and found a good agreement between theoretical prediction and experimental measurement, given homogeneous, isotropic and elastic nature of scratched materials. Meng et al. [20] studied material removal mechanism and deformation characteristics of mono-crystal silicon carbide by using nanoscratching with Berkovich indenter, and found a high-pressure induced phase transformation during nanoscratching process. AlMotasem et al. [21] explored grain size dependence of wear response by carrying out molecular dynamics simulation of nanoscratching of nanocrystalline ferrite, and found an increase in the friction coefficient with increasing normal load.

The friction coefficient is a key parameter in designing mechanical systems with contacting surfaces, and modelling performance of system such as friction-induced vibration, efficiency of gear transmission [22], mechanism of lubrication [23, 24] and comfort of soft contact lenses [25]. However, modelling frictional behaviour is not simple, since friction force depends on various parameters such as surface roughness, microscaled surface texture [26, 27], true contact area [28], normal load, dynamic behaviour of contact interface with vibration [29], material [30, 31], material transfer [32], sample thickness [33], test configurations and sliding systems [34–36]. Miyake and Yamazaki [6] investigated

✉ Ming Liu
mingliu@fzu.edu.cn

[1] School of Mechanical Engineering and Automation, Fuzhou University, Fuzhou 350116, People's Republic of China

scratching properties of extremely thin diamond-like carbon films by nanoscratch test with Berkovich indenter, and found the friction coefficient increased for scratching in the corn direction, while decreased for scratching in the edge direction as normal load increased. Maegawa et al. [37] studied the effect of normal load on the friction coefficient for sliding contact, and found the friction coefficient decreased with increasing load for rubber specimens. Yamaguchi et al. [38] investigated the effect of porosity on dry sliding friction of polymer foam blocks under different normal loads, and elucidated the increase in the friction coefficient with increasing porosity by a contact model considering elastic collapse [39] and friction-induced torque [40, 41]. In this study, effects of normal load on the measured friction coefficient by microscratch test were studied with a spherical indenter. A purely geometrical intersection model was used to rationalise the increase in the friction coefficient with increasing normal load. Furthermore, stress state of the material under contact during scratch test was discussed.

2 Microscratch Experimental Procedure

Microscratch test was carried out under normal loads ranging from 0.01 to 1 N. Anton Paar OPX system with microscratch tester MST[2] and force feedback loop control was used under conditions of a constant normal load, a constant speed and dry contact with Rockwell C 120° diamond indenter of spherical radius 100 μm. The commercially available copper sample with cubic geometry of side length 20 mm was chosen, since copper is soft and easy to deform plastically. The diamond indenter can be assumed to be rigid compared with copper, the indenter damage is negligible and the same indenter was used for all scratch tests in this study. The procedure was the same as that presented in References [18, 19]. True penetration and residual depths were measured by prescan and postscan before and after the scratch test along the same scratch track [4], and the surface of sample was viewed as the baseline for deformation [42]. Experimental parameters for scratch tests were as follows: scratch length was 200 μm; scratch test lasted 30 s; scanning load for prescan and postscan was 5 mN; acquisition rate was 30 Hz. Profiles of the sample before and after scratching were measured during prescan and postscan under a low load (i.e. 5 mN), respectively. The vertical displacement of the probe was monitored by the displacement sensor before, during and after a scratch, and the measurement was probe-based. The surface profile was measured during the prescan process with the origin located at the initial contact point, and the surface height was regarded to increase when the probe lowered into the sample. The applied normal load during prescan and postscan was significantly low (i.e. 5 mN), resulting in negligible deformation compared with that during the scratch test. Penetration and residual depths were obtained by subtracting the surface profile: the difference between the surface profile during scratch process and that during prescan determined the penetration depth; the difference between the surface profile during postscan and prescan determined the residual depth. The depth was regarded to be positive when the indenter was pushed into the specimen. Scratch tests were carried out in dry ambient laboratory condition: 23 °C and 50% relative humidity. The effect of instrument frame compliance is negligible for microscratch test under relatively large loads. Rockwell C 120° diamond indenter used in the present study is a cone of half-apex angle that ends into a hemispherical tip of radius $R = 100$ μm with a transition depth $d_t = R(1 - \sin\theta) = 100(1 - \sin 60°) \approx 13.4$ μm [4], see Fig. 1.

3 Results and Discussion

Figure 2 shows the variation of experimentally measured variables with position during the scratch test under a constant normal load condition. The friction coefficient μ is taken as the ratio of tangential force F_t over normal force F_n [43].

$$\mu = \frac{F_t}{F_n}. \tag{1}$$

The positive depths are due to the indenter being pushed into the specimen. The noisy data indicate stick–slip phenomenon [18, 44]. Since variables keep fluctuating during the scratch process, their average values are used and computed as the ratio of the integration over a certain distance range over the range length

$$\bar{x} = \frac{\int_{l_{\min}}^{l_{\max}} x \mathrm{d}l}{l_{\max} - l_{\min}}, \tag{2}$$

where x is the measured value varying with position. Three repeated tests were carried out under the same normal load; the statistical variation was negligibly small and the average value was used for analysis.

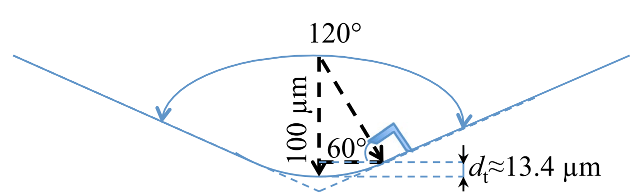

Fig. 1 Schematic illustration of Rockwell C 120° indenter with spherical tip of radius 100 μm

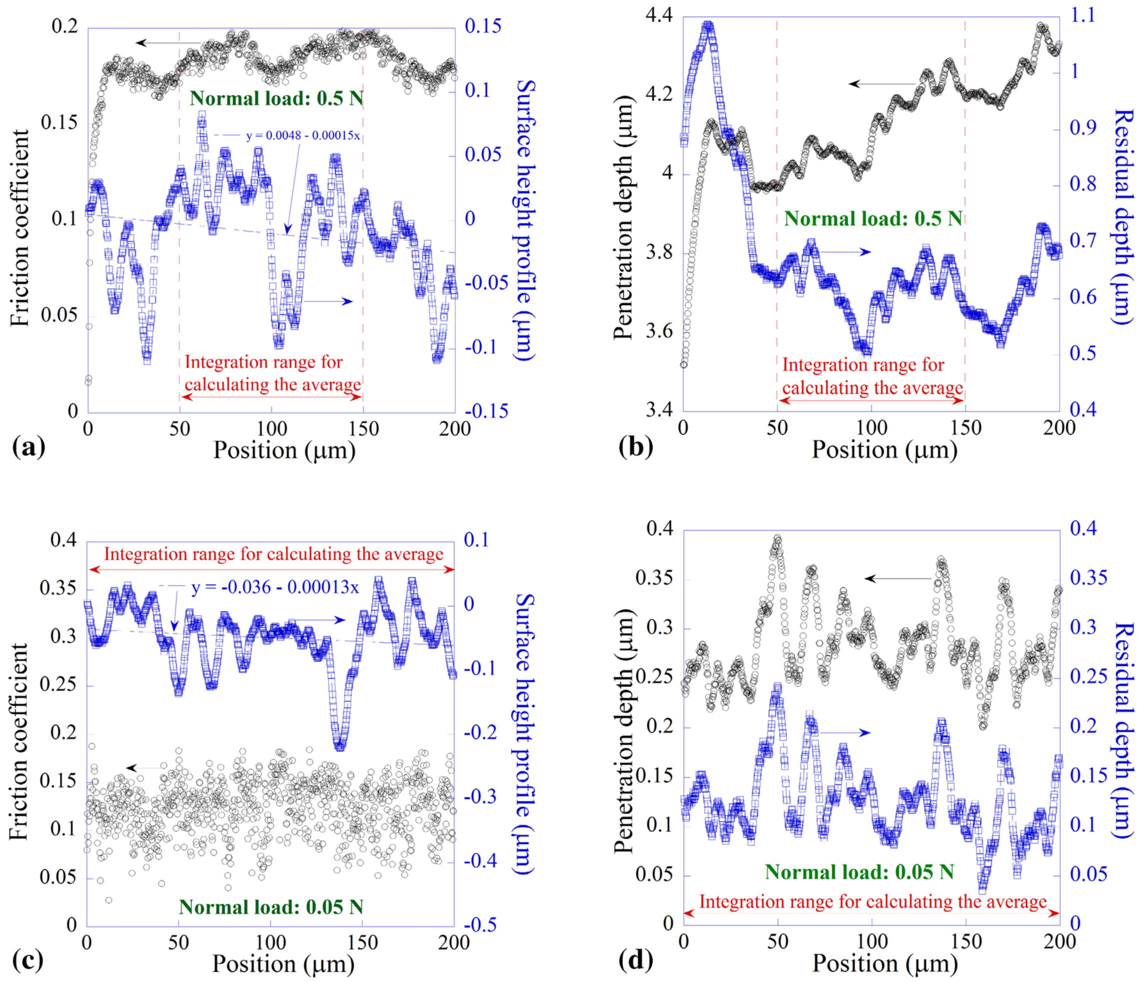

Fig. 2 The variation of experimentally measured variables with position during the scratch test under a constant normal load: **a** the friction coefficient and the surface profile height under a normal load of 0.5 N; **b** penetration and residual depths under a normal load of 0.5 N; **c** the friction coefficient and the surface profile height under a normal load of 0.05 N; **d** penetration and residual depths under a normal load of 0.05 N

Under a relatively large normal load (e.g. 0.5 N), the friction coefficient increases abruptly during the initial stage, which is usually observed in experiment [39], and the data during the initial stage are not used for calculating the average value. Under a relatively small normal load (e.g. 0.05 N), the fluctuation amplitude of the friction coefficient during the initial stage is almost the same as that for the whole process, and all the data during the scratch test are used for calculating the average value. The integration range for calculating the average value is from 50 to 150 μm for normal loads larger than 0.3 N; and all the data from 0 to 200 μm are used for integration for normal loads smaller than 0.3 N. The effect of the sample tilt can be neglected, since the absolute value of the slope is smaller than 0.00015 under a linear fitting of the surface height profile, see Fig. 2a and c.

Figure 3 shows the dependence of measured variables, which are calculated by averaging the fluctuating data after integration according to Eq. (2). All variables including the friction coefficient μ, penetration depth d_p, residual depth d_r, elastic recovery depth d_e and contact depth h_c increase with increasing normal load F_n. Power-law functions are found to be applicable to fit dependences of those variables on normal load. The friction coefficient was found to decrease with increasing normal load for foam blocks [39] due to elastic collapse [39] and friction-induced torque [40, 41]. The friction coefficient of sliding contact was also found to decrease with increasing normal load for rubber specimen that is elastic [37]. The friction coefficient was found to be nearly constant and independent of normal load under nanoscratching of amorphous carbon films with point-on direction of Berkovich indenter [18]. Nevertheless, for solid blocks with plastic deformation, our result of copper under microscratch with a spherical indenter shows that the friction coefficient

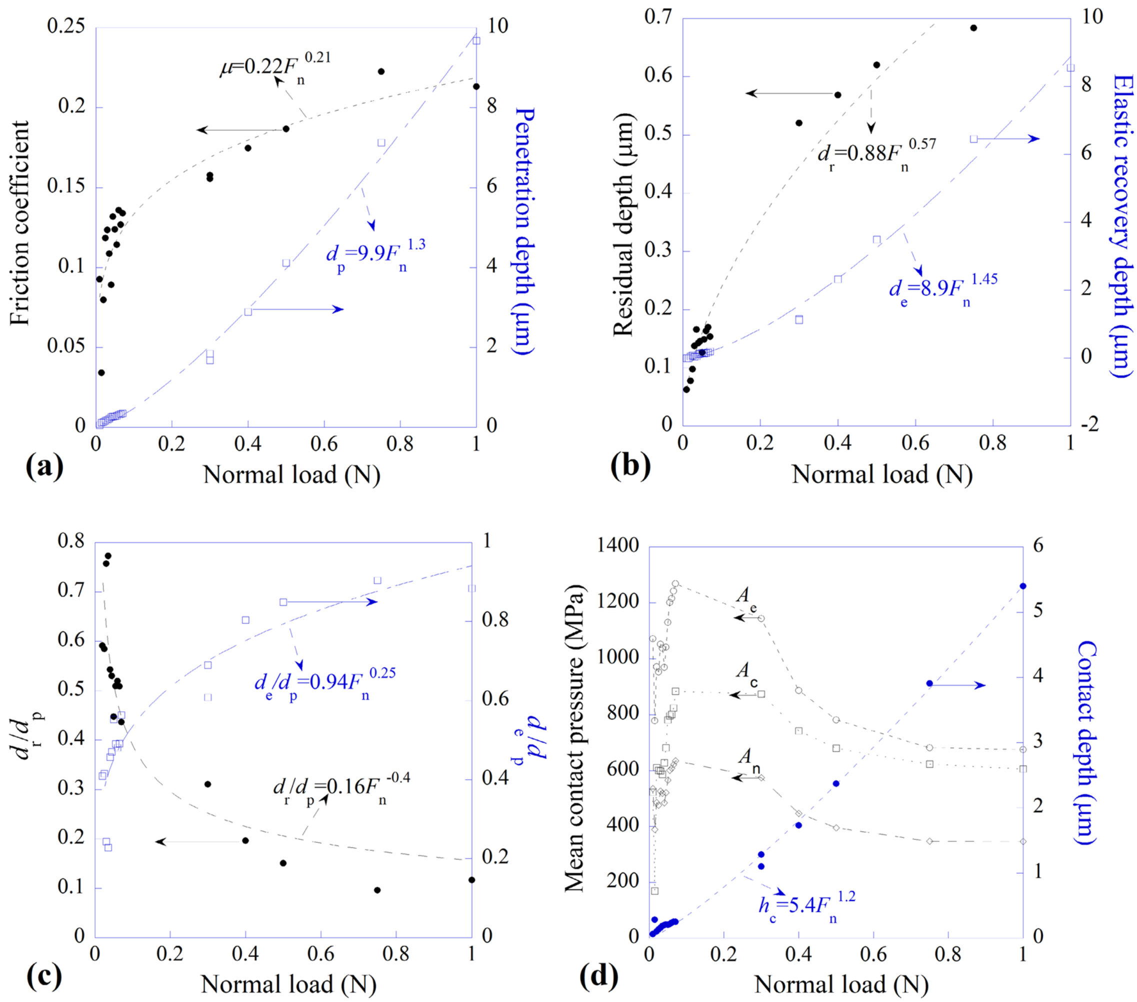

Fig. 3 The variation of measured variables with normal load F_n: **a** the friction coefficient μ and penetration depth d_p; **b** residual depth d_r and elastic recovery depth d_e; **c** d_r/d_p and d_e/d_p; **d** mean contact pressures calculated from different contact areas from Eqs. (4, 5, 7) and contact depth from Eq. (6)

increases with increasing normal load, which is consistent with molecular dynamics simulation of nanoscratching of nanocrystalline ferrite [21]. The increase of the friction coefficient is mainly due to the ploughing effect with the increase in dislocation density [21], which is attributed to plastic deformation, and increases with normal load and penetration depth; see the solid curve representing the ploughing component of the friction coefficient in Fig. 5.

Elastic recovery depth is just penetration depth minus residual depth

$$d_e = d_p - d_r. \tag{3}$$

The maximum penetration depth under the maximum normal load (i.e. 1 N) is about 10 μm, which is smaller than d_t, see Fig. 3a. Thus, it is only the spherical part that makes contact with the sample during scratch test for the normal loads applied.

Penetration depth d_p represents the total deformation amount with elastic depth d_e and residual depth d_r representing elastic and plastic deformation amounts, respectively [19]. Figure 3c displays variations of elastic/total and plastic/total with normal load. d_e/d_p increases, while d_r/d_p decreases with increasing normal load, revealing the significant amount of elastic deformation, although penetration depth becomes larger, and scratched trace becomes broader with increasing normal load. Elastic deformation is believed to predominate in the total deformation and control the contact response during scratching.

Mean contact pressure, p_n, can be determined as normal load divided by the projected contact area, which is assumed to be a half circle during scratch test and consisting with the definition of scratch hardness [2]. The nominal contact area A_n is determined by purely geometrical intersection, and penetration depth d_p is used as the contact depth

$$A_n = \frac{\pi d_p(2R - d_p)}{2}, \quad (4)$$

where R is the radius of spherical indenter.

The true contact area is determined by contact depth, which is only half of penetration depth for purely elastic contact [45], and

$$A_e = \frac{\pi d_p(4R - d_p)}{8}, \quad (5)$$

where A_e is the contact area from purely elastic contact model.

For elastic–plastic contact deformation, the contact depth, which represents the plastic component of total displacement, can be calculated as [46]

$$h_c = \frac{d_p + d_r}{2}. \quad (6)$$

Therefore, the true projected contact area A_c can be calculated as

$$A_c = \frac{\pi(d_p + d_r)(4R - d_p - d_r)}{8}. \quad (7)$$

Mean contact pressures calculated from three different contact areas abruptly increase for relatively low loads, and then slowly decrease for relatively large loads; see Fig. 3d. Under large normal loads, the mean contact pressure calculated from A_c is close to that calculated from A_e, since the residual depth becomes relatively smaller and almost negligible compared with penetration depth, and $h_c \approx d_p/2$. d_r/d_p decreases with increasing normal load for large normal loads, and a smaller d_r/d_p indicates a more prominent role of elastic deformation with a diminishing contribution from plastic deformation. The deformation is more likely to be elastic-dominated under a smaller d_r/d_p. The decrease in mean contact pressure under large normal loads is attributed to plastic deformation, while contribution of plastic deformation into the total deformation becomes smaller under large normal loads. It is believed that plastic deformation during scratch is mainly constrained within the surface region.

Assume purely elastic deformation at normal load of 1 N with penetration depth 9.674 μm, since d_r/d_p at normal load 1N is very low (about 0.1). Elastic modulus can be obtained by Hertzian solution as [45]

$$E_r = \frac{1}{\frac{1-\nu_s^2}{E_s} + \frac{1-\nu_i^2}{E_i}} = \frac{3P}{4R^{0.5}d_p^{1.5}}, \quad (8)$$

where E and ν are elastic modulus and Poisson's ratio, respectively; and the subscripts "s" and "i" indicate the sample and the indenter, respectively; d_p is equivalent to indentation displacement and P is twice the normal load (i.e. 2N) under the assumption that the projected contact area is only a half circle for scratch test, since Hertzian solution requires a whole circle as the contact area. With $E_i = 1141$ GPa, $\nu_i = 0.07$ for diamond indenter [47], $\nu_s = 0.335$ for copper [48] and $R = 100$ μm, E_s is calculated to be about 4.4 GPa, which is much smaller than the true value of copper. Although loading curves in nanoindentation and nanoscratch testes are very similar at low loads [49], loading curves in the microscratch test are different from those in the indentation test at relatively large loads, and tangential loading in the microscratch test can produce larger penetration depths at relatively larger loads compared with the indentation test under the same normal load. It is the contributions from the lateral force and higher energy transfer due to moving line contact between indenter and specimen [50] in the scratching test that alter stress distribution [11] and make $P/d_p^{1.5}$ not so large as that (no less than 100 GPa) in purely elastic case [48], and E_s is underestimated. The lateral force can produce contact pressure in the thrusting direction and adhesion shear stress on the contact area, which can serve as residual stresses and influence normal contact response. Moreover, the tangential load in the scratch test can promote yielding, resulting in greater penetration depths at higher loads compared with indentation [49], which rationalises the smaller values $P/d_p^{1.5}$due to larger d_p in the scratch test than that in the indentation test.

Frictional force is the sum of adhesion force and deformation force [51]. The friction coefficient also composes of adhesion and ploughing components. Adhesion friction is proportional to the interfacial shear strength and the real contact area. Ploughing friction coefficient is mainly determined by the ratio of the projected contact area in the thrust (i.e. horizontal) direction over the projected contact area in the cutting (i.e. vertical) direction.

Based on the geometrical intersection model shown in Fig. 4, the projected contact area, S_h, in the thrusting (or horizontal) direction, and the projected contact area, S_v, in the cutting (or vertical) direction, can be calculated based on the area of a circle segment formed by the arch and chord, and the area of half a circle, respectively, as

$$S_h = \frac{R^2}{2}(\phi - \sin\phi), \ S_v = \frac{\pi d_p(2R - d_p)}{2}, \quad (9)$$

where R is the radius of spherical indenter, ϕ is the central angle in radians and

$$\cos\frac{\phi}{2} = \frac{R - d_p}{R}, \ \sin\frac{\phi}{2} = \frac{\sqrt{(2R - d_p)d_p}}{R}, \quad (10)$$

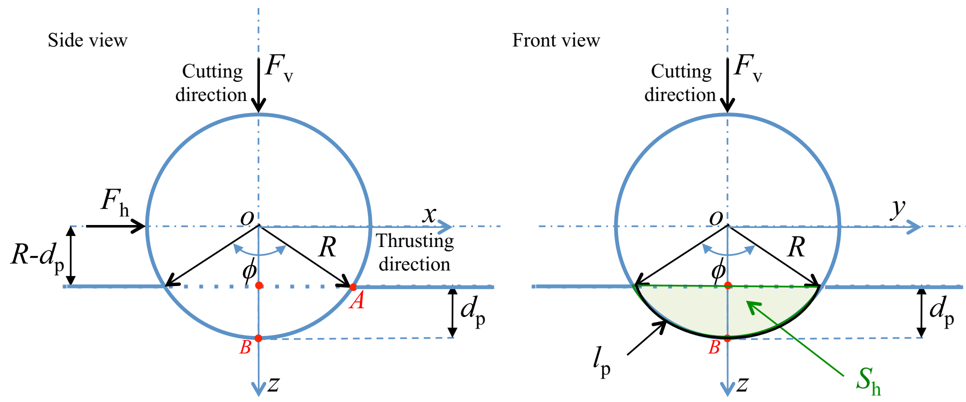

Fig. 4 Schematic of a spherical indenter scratching on a flat based on the geometrical intersection (x is the scratch direction, l_p is the perimeter length, S_h is the projected contact area bearing horizontal load)

where d_p is the penetration depth, and $d_p < R$ in experiment. Input of Eq. (10) into Eq. (9) with $\sin\phi = 2\sin(\phi/2)\cos(\phi/2)$ gives

$$S_h = R^2 \arccos\frac{R-d_p}{R} - \left(R-d_p\right)\sqrt{\left(2R-d_p\right)d_p}. \tag{11}$$

The perimeter length l_p is equal to the arc length

$$l_p = 2R\arccos\frac{R-d_p}{R}. \tag{12}$$

The ratio of the projected contact area in the horizontal direction over the projected contact area in the vertical direction is related to the friction coefficient component due to ploughing deformation

$$\frac{S_h}{S_v} = \frac{2R^2\arccos\frac{R-d_p}{R} - 2\left(R-d_p\right)\sqrt{\left(2R-d_p\right)d_p}}{\pi d_p\left(2R-d_p\right)}. \tag{13}$$

Figure 5 shows the variation of S_h/S_v based on the purely geometrical intersection model Eq. (13) with penetration depth. Experimentally measured friction coefficients, which are the apparent friction coefficient, are also included in Fig. 5. Since the apparent friction coefficient μ composes of both adhesion and ploughing components, and S_h/S_v only represents ploughing component, μ is found to be larger than S_h/S_v, which is reasonable. Adhesion friction component is expected to be as prominent as ploughing friction component, since copper, which is a soft metal, can be used to clean the indenter (i.e. remove the dirt on indenter surface by making indents in copper).

d_p can be replaced by h_c in order to consider the deformation, since it is contact depth rather than penetration depth that determines the contact geometry, and

$$\frac{S_h}{S_v} = \frac{2R^2\arccos\frac{R-h_c}{R} - 2\left(R-h_c\right)\sqrt{\left(2R-h_c\right)h_c}}{\pi d_c\left(2R-h_c\right)} \tag{14}$$

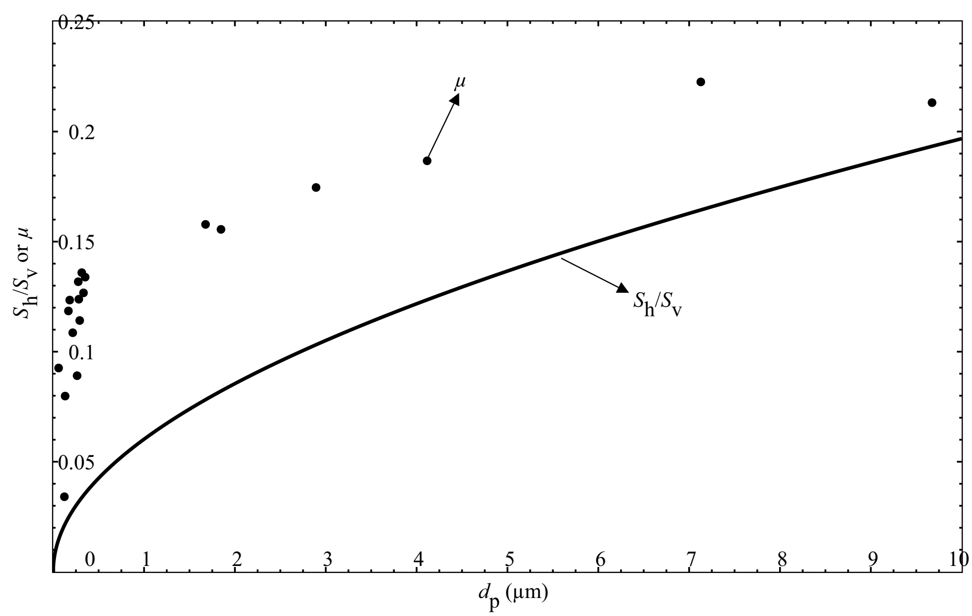

Fig. 5 Plot of the ratio S_h/S_v as a function of penetration depth based on the geometrical intersection model. Equation (13) is represented by a solid line; and experimentally measured friction coefficient data are denoted by filled circles

$$S_{\mathrm{h}} = R^2 \arccos \frac{R - h_{\mathrm{c}}}{R} - (R - h_{\mathrm{c}}) \sqrt{(2R - h_{\mathrm{c}}) h_{\mathrm{c}}}, S_{\mathrm{v}} = \frac{\pi h_{\mathrm{c}} (2R - h_{\mathrm{c}})}{2} \tag{15}$$

where $h_{\mathrm{c}} = (d_{\mathrm{p}} + d_{\mathrm{r}})/2$ [46].

Since friction composes of adhesion and ploughing components, the lateral force also composes of adhesion and ploughing components correspondingly. The lateral mean contact pressure, p_{l}, can be calculated to be the ploughing component of lateral force F_{p} divided by the projected contact area in thrusting direction S_{h}. The adhesion mean contact stress over the contact area, p_{a}, can be calculated to be the adhesion component of lateral force F_{a} divided by the projected contact area in cutting direction S_{v}. Therefore,

$$p_{\mathrm{l}} = \frac{F_{\mathrm{p}}}{S_{\mathrm{h}}}, p_{\mathrm{a}} = \frac{F_{\mathrm{a}}}{S_{\mathrm{v}}}. \tag{16}$$

Assume adhesion component of lateral force is proportional to the projected contact area in the vertical direction, and ploughing component of lateral force is proportional to the projected contact area in the horizontal direction, the apparent friction coefficient is expressed as

$$\mu = \frac{F_{\mathrm{l}}}{F_{\mathrm{n}}} = \frac{F_{\mathrm{a}} + F_{\mathrm{p}}}{F_{\mathrm{n}}} = \frac{p_{\mathrm{a}} S_{\mathrm{v}} + p_{\mathrm{l}} S_{\mathrm{h}}}{F_{\mathrm{n}}}, F_{\mathrm{a}} = p_{\mathrm{a}} S_{\mathrm{v}}, F_{\mathrm{p}} = p_{\mathrm{l}} S_{\mathrm{h}}, \tag{17}$$

where F_{l} is the total lateral force, F_{a} and F_{p} are adhesion and ploughing components of lateral force F_{l}, respectively; p_{a} and p_{n} are adhesion mean contact stress and lateral mean contact pressure, respectively, which are dependent on normal load and contact depth, since elastic and plastic contributions keep changing with varying loads. The ploughing component μ_{p} of the friction coefficient can be calculated as $\mu_{\mathrm{p}} = F_{\mathrm{p}}/F_{\mathrm{n}}$. Assume ploughing component μ_{p} of the friction coefficient is equal to the ratio of the projected contact area in the horizontal direction S_{h} over the projected contact area in the vertical direction S_{v}, $\mu_{\mathrm{p}} = S_{\mathrm{h}}/S_{\mathrm{v}}$, then

$$\mu_{\mathrm{p}} = \frac{F_{\mathrm{p}}}{F_{\mathrm{n}}} = \frac{S_{\mathrm{h}}}{S_{\mathrm{v}}} = \frac{p_{\mathrm{l}} S_{\mathrm{h}}}{p_{\mathrm{n}} S_{\mathrm{v}}} \Rightarrow p_{\mathrm{l}} = p_{\mathrm{n}}. \tag{18}$$

It is found that the lateral mean contact pressure p_{l} is equal to the normal mean contact pressure p_{n}, which means scratch hardness is equal to indentation hardness if mean contact pressure is regarded to be hardness. The equality between lateral and normal mean contact pressures is consistent with the assumption of using $S_{\mathrm{h}}/S_{\mathrm{v}}$ as the ploughing friction coefficient that the forces required to push bulk material are identical in both normal and lateral directions [52]. Assume plane strain condition on *x-o-z* plane with the out-of-plane direction being perpendicular to both scratch and vertical directions defined in Fig. 4, and the adhesion shear stress is small and can be neglected, then $\sigma_x = \sigma_z = -p_{\mathrm{n}}$, $\sigma_y = (\sigma_x + \sigma_z)/2 = -p_{\mathrm{n}}$ (negative signs indicate compressive stresses) under plastic deformation, resulting in a hydrostatic compressive stress state for the material under the indenter for the scratch test. Since stress state is also triaxial compressive for indentation, and fully plastic indentation theory and elastic Hertzian indentation theory have been utilised in analysing scratch tests [53–55], plastic deformation processes for scratch and indentation tests are believed to be similar with common features, and the two techniques are closely related with similar morphologies of plastic deformation [8]. It is worth noting that the equivalence of scratch hardness and indentation hardness requires the use of ploughing component of lateral force, which is only a portion of the total lateral force. If the total lateral force would be used, then the calculated scratch hardness would be larger than indentation hardness. Moreover, indentation hardness was found to be more than twice the scratch hardness by a spherical indenter from molecular dynamics simulation of nanoscratching of nanocrystalline ferrite due to pile-up formation [21]. Nevertheless, a good correlation between scratch hardness and nanoindentation hardness was found for copper thin films at low indentation depths under Berkovich indenter with the total included angle of 142.3° [2], since there was no pile-up or sink-in at low load indents [56]. The purely geometrical intersection model does not consider pile-up formation in the front and sideways of the indenter, and might overestimate scratch hardness. It is worth noting that hardness is associated with fully developed plastic deformation, but elastic deformation predominates in the total deformation for the scratch test with a spherical indenter, precluding the direct comparison of hardness obtained by scratch with a sphere with those obtained by sharp indenters.

Input of Eq. (18) into Eq. (17) gives

$$p_{\mathrm{a}} = \left(\mu - \frac{S_{\mathrm{h}}}{S_{\mathrm{v}}}\right) p_{\mathrm{n}}, \tag{19}$$

where μ and F_{n} can be experimentally measured in the scratch test; S_{h} and S_{v} are calculated from contact depth according to Eq. (15). Adhesion component of friction, μ_{a}, is just the term in parenthesis $(\mu_{\mathrm{a}} = \mu - S_{\mathrm{h}}/S_{\mathrm{v}})$. Figure 6a and b shows the variation of adhesion mean shear stress p_{a} over the contact area and adhesion friction coefficient μ_{a}, respectively, with normal load. The adhesion mean shear stress firstly increases under small loads, and then decreases under large loads with increasing normal load. Adhesion mean shear stress is much lower than mean contact pressure. The adhesion friction coefficient decreases with increasing normal load, and approaches a constant value under large normal loads due to the predominant contribution of elastic deformation into the total deformation. It is believed that under elastic deformation or significant contribution of

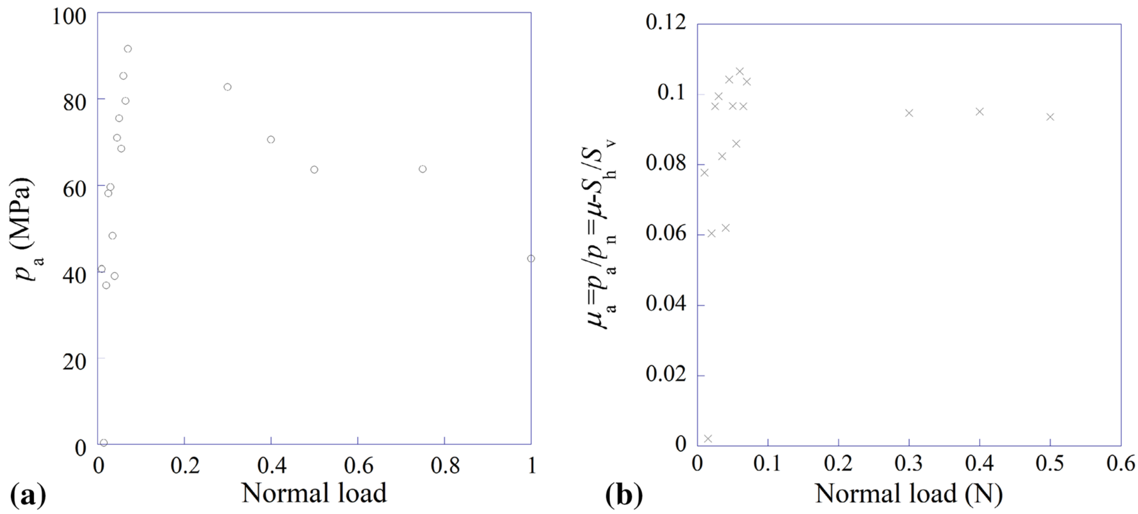

Fig. 6 The variation of **a** adhesion shear stress calculated by Eq. (19); and **b** the adhesion component of the apparent friction coefficient with normal load. S_h/S_v is calculated by Eq. (14)

elastic deformation into the total deformation, the adhesion friction coefficient is constant. Plasticity is a grand equaliser that renders a uniform distribution of stress over the contact region [57]. If significant plastic deformation is not developed, stress distribution cannot be uniform. Fully developed plastic deformation is associated with mean contact pressure that is three times yield stress [58]. Yield stress of copper used in the present work should not be larger than 100 MPa. Mean contact pressure should be less than 300 MPa if fully plastic deformation would be developed. Figure 3d displays that mean contact pressures, which can be regarded as indentation hardness, are more than 600 MPa (larger than three times yield stress) under large normal loads, which can be explained by noting a significant contribution of elastic deformation into the total deformation for the scratch test with a spherical indenter, since fully plastic deformation is not developed. It is the spherical indenter that results in a less developed plastic deformation and a larger mean contact pressure due to the significant elastic deformation.

If adhesion shear stress is considered as shear stress τ_{zx}, and mean contact pressures in normal and lateral directions are considered to be normal stresses σ_x and σ_z, the principal stresses in x-o-z plane, see Fig. 7, can be obtained from the two-dimensional state of stress $\sigma_x = \sigma_z = -p_n$, $\tau_{xz} = -p_a$ (where negative signs indicate compressive stresses, the reason of the negative sign of shear stress is that τ_{xz} can turn the body anti-clockwise)

$$\left.\begin{matrix}\sigma_{\max}\\ \sigma_{\min}\end{matrix}\right\} = \frac{\sigma_x+\sigma_z}{2} \pm \sqrt{\left(\frac{\sigma_x-\sigma_z}{2}\right)+\tau_{xz}^2} = -p_n \pm p_a, \quad (20)$$

$$\tan\alpha = \frac{\tau_{xz}}{\sigma_x - \sigma_{\min}} = 1 \Rightarrow \alpha = 45^\circ, \quad (21)$$

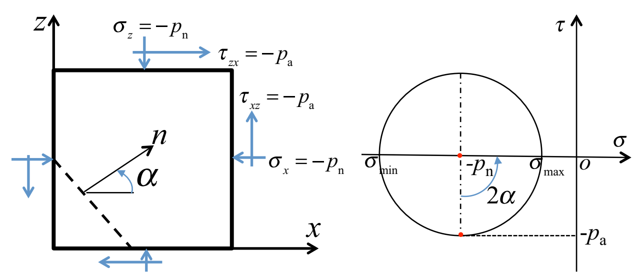

Fig. 7 Stress state with Mohr's stress circle of the material under contact during scratch test

where α is the principal angle defined in Fig. 7.

For plane strain condition under plastic deformation,

$$\sigma_y = (\sigma_{\max} + \sigma_{\min})/2 = -p_n. \quad (22)$$

Based on von Mises criterion and plane strain condition, plastic deformation initiates when

$$\sigma_{\max} - \sigma_{\min} = \frac{2}{\sqrt{3}}\sigma_y, \quad (23)$$

where σ_y is yield stress and no more than 90 MPa for the copper used.

Combine Eqs. (20) and (23), which gives the criterion of plastic initiation during the scratch deformation

$$p_a = \frac{\sigma_y}{\sqrt{3}}, \quad (24)$$

with σ_y = 90 MPa, which is the largest possible value, $p_a \approx 52$ MPa, which is comparable with the values shown in Fig. 6a. Although elastic deformation predominates in the total deformation, plastic deformation is expected for copper, which is evidenced by the larger residual depth under a larger normal load, see Fig. 3b. The critical value of p_a for yielding inception could be further smaller, since tangential loading with friction can promote yielding [59]. The reason why p_a shown in Fig. 6a is relatively large can be explained by work hardening of material, which is expected for soft copper [60], since σ_y becomes the flow stress after plastic yielding, and increases with straining, making p_a larger by Eq. (24).

Based on linear elastic fracture mechanics [61] with the assumption of existence of semi-circular horizontal crack plane emanating from the probe tip [4], the lateral force F_l is related to the perimeter length l_p and horizontally projected contact area S_h by [62–64]

$$\frac{F_l}{\sqrt{2l_pS_h}} = K_c, \tag{25}$$

where K_c is fracture toughness. With Eqs. (11) and (12), a geometry function can be defined as

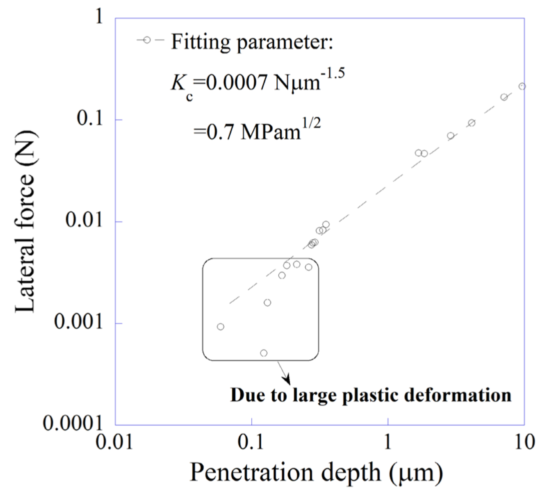

Fig. 8 Proportional relationship between lateral force F_l and penetration depth. Lateral force is obtained from Eq. (1) and $F_l = \mu F_n$

copper with a spherical indenter under small normal loads, since crack plane is absent during the scratch test of soft copper. Although the proportionality between F_l and d_p still holds for the case without fracture, the fitting parameter K_c should not have the physical meaning of fracture toughness.

$$g\left(\frac{d_p}{R}\right) = 2l_pS_h = 4R^3 \arccos\left(1-\frac{d_p}{R}\right)\left[\arccos\left(1-\frac{d_p}{R}\right) - \left(1-\frac{d_p}{R}\right)\sqrt{\left(2-\frac{d_p}{R}\right)\frac{d_p}{R}}\right]. \tag{26}$$

From Taylor series expansion, under small values of d_p/R, Eq. (26) can be simplified to

$$g\left(\frac{d_p}{R}\right) \approx \frac{32}{3}R^3\left(\frac{d_p}{R}\right)^2 \text{ for } \frac{d_p}{R} \ll 1. \tag{27}$$

Input of Eq. (27) into Eq. (25) gives

$$F_l = 4d_pK_c\sqrt{\frac{2}{3}R} \text{ for } d_p \ll R, \tag{28}$$

which predicts a proportional relationship between lateral force and penetration depth. Figure 8 displays dependence of lateral force on penetration depth obtained from scratch tests under various normal loads. d_p is smaller than 10 μm, which is much smaller than radius R, which is 100 μm, of spherical indenter. Therefore, $d_p \ll R$ required in Eq. (28) is fulfilled. The proportional relationship between F_l and d_p is consistent with theoretical prediction with fitting parameter $K_c \approx 0.7$ MPa·m$^{1/2}$, which is much smaller than the reasonable value (should be larger than 10 MPa·m$^{1/2}$ [65]) of fracture toughness for copper. Equation (28) is based on fracture mechanics under the assumption of crack plane in front of the probe tip, which is not satisfied for the scratch test of soft K_c in Eq. (28) represents deformation or shearing resistance toughness under non-fracture condition rather than fracture toughness. Under large penetration depths or normal loads, elastic deformation predominates in the total deformation, see Fig. 3c, resulting in excellent agreement between experimental measurement and theoretical prediction, which can be explained by noting that Eq. (28) is based on elastic mechanics without considering plasticity. Nevertheless, under small penetration depths or normal loads, plastic deformation is more significant than elastic deformation, see Fig. 3c; lateral force is not proportional to penetration depth, which is highlighted in Fig. 8, and can be explained by noting that the proportionality relation is predicted under the condition of negligible plastic deformation and Eq. (28) is not applicable, given the significant contribution of plastic deformation in the total deformation.

Figure 9 shows multi-focus optical images of imprints after scratch tests under two different normal loads 0.7 N and 0.25 N. The width of the trace increases with increasing normal load. The hemispherical edges at the start and end points are caused by the spherical shape of the probe. Shear bands can be observed along the border of the trace. Both sides of the trace are not perfectly straight, which could be

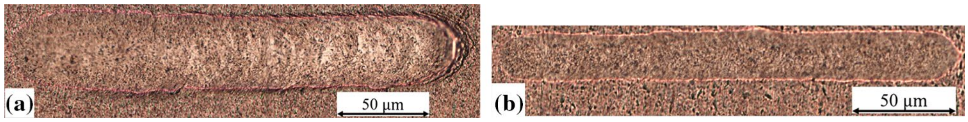

Fig. 9 Optical images of imprints after scratch tests of scratch length 200 µm for two different normal loads: **a** $F_n = 0.7$ N; **b** $F_n = 0.25$ N

due to the pile-up of soft copper in front of the probe. If scratch width w is estimated by Intersecting Chord Theorem

$$w = \sqrt{(2R - d_p)d_p}, \tag{29}$$

where d_p is the residual depth, and R is the radius of spherical probe. With R = 100 µm, and $d_r = 1.6$ µm for $F_n = 0.7$ N, $d_r = 0.6$ µm for $F_n = 0.25$ N, it can be calculated that $w = 18$ µm for $F_n = 0.7$ N, $w = 11$ µm for $F_n = 0.25$ N, which are much smaller than the experimental measurements from the optical traces, ($w = 38$ µm for $F_n = 0.7$ N, $w = 23$ µm for $F_n = 0.25$ N in Fig. 9). Since pile-up is expected not only in front of the probe, and also along both sides of the scratch, the pile-up contact width, which is the distance from the groove-wall zero point to the pile-up maximum height [52], makes the scratch width a little larger than the estimation based on purely geometrical intersection.

4 Conclusions

The microscratch test was carried out to study the effect of normal load on the measured friction coefficient. The soft copper was chosen and a constant normal load was applied during the scratch. Since the measured data keep fluctuating along the scratch track, the average value is used for further analysis. The friction coefficient is found to increase with increasing normal load, which is elucidated by a purely geometrical intersection model. Elastic deformation predominates in the total deformation as normal load becomes larger, which is evidenced by the increase in the ratio of elastic recovery depth over penetration depth as well as the decrease in the ratio of residual depth over penetration depth with increasing normal load. Stress state of the scratched material within the contact region is discussed under assumption of plane strain condition. The pressure in the normal direction is found to be the same as that in the lateral direction. The adhesion shear stress is regarded as the shear stress and is much smaller than normal stress. It is the adhesion shear stress acting on the contact surface that causes plastic deformation. The material experiencing scratch-induced deformation is under hydrostatic compressive stress state. Under large normal loads, elastic deformation predominates in the total scratch-induced deformation. The lateral force is found to be proportional to penetration depth for spherical indenter with the fitting parameter representing deformation or shearing resistant toughness.

Acknowledgements This project is supported by National Natural Science Foundation of China (Grant Nos. 51705082 and 51875106) and Fujian Provincial Collaborative Innovation Center for High-end Equipment Manufacturing (No. 0020-50006103). M. Liu is also grateful for the support from Fujian Provincial Minjiang Scholar Program (N0. 0020-510486).

References

1. Venkataraman, S., Kohlstedt, D.L., Gerberich, W.W.: Microscratch Analysis of the Work of Adhesion for Pt Thin-Films on NiO. J. Mater. Res. **7**(5), 1126–1132 (1992). https://doi.org/10.1557/Jmr.1992.1126
2. Beegan, D., Chowdhury, S., Laugier, M.T.: Comparison between nanoindentation and scratch test hardness (scratch hardness) values of copper thin films on oxidised silicon substrates. Surf. Coat. Technol. **201**(12), 5804–5808 (2007). https://doi.org/10.1016/j.surfcoat.2006.10.031
3. Wredenberg, F., Larsson, P.L.: Scratch testing of metals and polymers: Experiments and numerics. Wear. **266**(1–2), 76–83 (2009). https://doi.org/10.1016/j.wear.2008.05.014
4. Akono, A.T., Randall, N.X., Ulm, F.J.: Experimental determination of the fracture toughness via microscratch tests: Application to polymers, ceramics, and metals. J. Mater. Res. **27**(2), 485–493 (2012). https://doi.org/10.1557/jmr.2011.402
5. Bard, R., Ulm, F.J.: Scratch hardness—strength solutions for cohesive-frictional materials. Int. J. Numer. Anal. Methods Geomech. **36**(3), 307–326 (2012)
6. Miyake, S., Yamazaki, S.: Nanoscratch properties of extremely thin diamond-like carbon films. Wear. **305**(1–2), 69–77 (2013). https://doi.org/10.1016/j.wear.2013.05.005
7. Wang, Z., Zeng, Q., Zheng, J.: Adsorption and Lubricating Behavior of Salivary Pellicle on Dental Ceramic. Lubrication Engineering: (2017)
8. Burnett, P.J., Rickerby, D.S.: The relationship between hardness and scratch adhession. Thin Solid Films **154**(1–2), 403–416 (1987)
9. Ollendorf, H., Schneider, D.: A comparative study of adhesion-test methods for hard coatings. Surf. Coat. Technol. **113**(1–2), 86–102 (1999). https://doi.org/10.1016/S0257-8972(98)00827-5
10. Matthews, A., Franklin, S., Holmberg, K.: Tribological coatings: contact mechanisms and selection. J. Phys. D **40**(18), 5463–5475 (2007). https://doi.org/10.1088/0022-3727/40/18/S07
11. Bhushan, B., Gupta, B.K., Azarian, M.H.: Nanoindentation, microscratch, friction and wear studies of coatings for contact recording applications. Wear **181**(95), 743–758 (1995)
12. Zhao, X.Z., Bhushan, B.: Material removal mechanisms of single-crystal silicon on nanoscale and at ultralow loads. Wear. **223**(1–2), 66–78 (1998). https://doi.org/10.1016/S0043-1648(98)00302-0
13. Beake, B.D., Goodes, S.R., Shi, B.: Nanomechanical and nanotribological testing of ultra-thin carbon-based and MoST films for

increased MEMS durability. J. Phys. D **42**(6), 065301 (2009). https://doi.org/10.1088/0022-3727/42/6/065301
14. Wu, T.W.: Microscratch and Load Relaxation Tests for Ultra-Thin Films. J. Mater. Res. **6**(2), 407–426 (1991). https://doi.org/10.1557/Jmr.1991.0407
15. Burnett, P.J., Rickerby, D.S.: The scratch adhesion test—an elastic–plastic indentation analysis. Thin Solid Films. **157**(2), 233–254 (1988). https://doi.org/10.1016/0040-6090(88)90006-5
16. Sekler, J., Steinmann, P.A., Hintermann, H.E.: The scratch test - different critical load determination techniques. Surf. Coat. Technol. **36**(1–2), 519–529 (1988). https://doi.org/10.1016/0257-8972(88)90179-X
17. Andriy, K., Yury, G., Vladislav, D., Ali, E.: Phase transformations in silicon under dry and lubricated sliding. Tribol. Trans. **45**(3), 372–380 (2002)
18. Charitidis, C., Logothetidis, S., Gioti, M.: A comparative study of the nanoscratching behavior of amorphous carbon films grown under various deposition conditions. Surf. Coat. Technol. **125**(1–3), 201–206 (2000). https://doi.org/10.1016/S0257-8972(99)00546-0
19. Huang, L.Y., Xu, K.W., Lu, J.: Evaluation of scratch resistance of diamond-like carbon films on Ti alloy substrate by nano-scratch technique. Diam. Relat. Mater. **11**(8), 1505–1510 (2002). https://doi.org/10.1016/S0925-9635(02)00054-7
20. Meng, B.B., Zhang, Y., Zhang, F.H.: Material removal mechanism of 6H-SiC studied by nano-scratching with Berkovich indenter. Appl. Phys. A. **122**(3), 247 (2016). https://doi.org/10.1007/s00339-016-9802-7
21. AlMotasem, A.T., Bergstrom, J., Gaard, A., Krakhmalev, P., Holleboom, L.J.: Atomistic insights on the wear/friction behavior of nanocrystalline ferrite during nanoscratching as revealed by molecular dynamics. Tribol. Lett. **65**(3), 101 (2017). https://doi.org/10.1007/s11249-017-0876-y
22. Diez-Ibarbia, A., Fernandez-Del-Rincon, A., Garcia, P., De-Juan, A., Iglesias, M., Viadero, F.: Assessment of load dependent friction coefficients and their influence on spur gears efficiency. Meccanica(3), 1–21 (2017)
23. Zhang, H.D., Takeuchi, Y., Chong, W.W.F., Mitsuya, Y., Fukuzawa, K., Itoh, S.: Simultaneous in situ measurements of contact behavior and friction to understand the mechanism of lubrication with nanometer-thick liquid lubricant films. Tribol. Int. **127**, 138–146 (2018). https://doi.org/10.1016/j.triboint.2018.05.043
24. Wang, J., Ma, L., Li, W., Zhou, Z.R.: Influence of different lubricating fluids on friction trauma of small intestine during enteroscopy. Tribol. Int. **126**, 29–38 (2018). https://doi.org/10.1016/j.triboint.2018.05.002
25. Sterner, O., Aeschlimann, R., Zurcher, S., Scales, C., Riederer, D., Spencer, N.D., Tosatti, S.G.P.: Tribological classification of contact lenses: From coefficient of friction to sliding work. Tribol. Lett. **63**(1), 9 (2016). https://doi.org/10.1007/s11249-016-0696-5
26. Zhang, S., Zeng, X., Igartua, A., Rodriguez-Vidal, E., van der Heide, E.: Texture design for reducing tactile friction independent of sliding orientation on stainless steel sheet. Tribol. Lett. **65**(3), 89 (2017). https://doi.org/10.1007/s11249-017-0869-x
27. Lu, P., Wood, R.J.K., Gee, M.G., Wang, L., Pfleging, W.: A novel surface texture shape for directional friction control. Tribol. Lett. **66**(1), 51 (2018). https://doi.org/10.1007/s11249-018-0995-0
28. Szlufarska, I., Chandross, M., Carpick, R.W.: TOPICAL REVIEW: Recent advances in single-asperity nanotribology. J. Phys. D **41**(12), 1854–1862 (2008)
29. Udaykant Jadav, P., Amali, R., Adetoro, O.B.: Analytical friction model for sliding bodies with coupled longitudinal and transverse vibration. Tribol. Int. **126**, 240–248 (2018). https://doi.org/10.1016/j.triboint.2018.04.018
30. Li, S., Li, Q., Carpick, R.W., Gumbsch, P., Liu, X.Z., Ding, X., Sun, J., Li, J.: The evolving quality of frictional contact with graphene. Nature. **539**(7630), 541–545 (2016). https://doi.org/10.1038/nature20135
31. Saravanan, P., Selyanchyn, R., Watanabe, M., Fujikawa, S., Tanaka, H., Lyth, S.M., Sugimura, J.: Ultra-low friction of polyethylenimine / molybdenum disulfide $(PEI/MoS_2)_{15}$ thin films in dry nitrogen atmosphere and the effect of heat treatment. Tribol. Int. **127**, 255–263 (2018). https://doi.org/10.1016/j.triboint.2018.06.003
32. Westlund, V., Heinrichs, J., Jacobson, S.: On the role of material transfer in friction between metals: initial phenomena and effects of roughness and boundary lubrication in sliding between aluminium and tool steels. Tribol. Lett. **66**(3), 97 (2018). https://doi.org/10.1007/s11249-018-1048-4
33. Lee, C., Li, Q., Kalb, W., Liu, X.Z., Berger, H., Carpick, R.W., Hone, J.: Frictional characteristics of atomically thin sheets. Science. **328**(5974), 76–80 (2010). https://doi.org/10.1126/science.1184167
34. Gabriel, P., Thomas, A.G., Busfield, J.J.C.: Influence of interface geometry on rubber friction. Wear. **268**(5–6), 747–750 (2010). https://doi.org/10.1016/j.wear.2009.11.019
35. Ben-David, O., Fineberg, J.: Static Friction Coefficient Is Not a Material Constant. Phys. Rev. Lett. **106**(25), 254301 (2011)
36. Zhou, C.J., Hu, B., Qian, X.L., Han, X.: A novel prediction method for gear friction coefficients based on a computational inverse technique. Tribol. Int. **127**, 200–208 (2018). https://doi.org/10.1016/j.triboint.2018.06.005
37. Maegawa, S., Itoigawa, F., Nakamura, T.: Effect of normal load on friction coefficient for sliding contact between rough rubber surface and rigid smooth plane. Tribol. Int. **92**, 335–343 (2015). https://doi.org/10.1016/j.triboint.2015.07.014
38. Yamaguchi, T., Sugawara, T., Takahashi, M., Shibata, K., Moriyasu, K., Nishiwaki, T., Hokkirigawa, K.: Effect of porosity and normal load on dry sliding friction of polymer foam blocks. Tribol. Lett. **66**(1), 34 (2018). https://doi.org/10.1007/s11249-018-0988-z
39. Yamaguchi, T., Sugawara, T., Takahashi, M., Shibata, K., Moriyasu, K., Nishiwaki, T., Hokkirigawa, K.: Dry sliding friction of ethylene vinyl acetate blocks: Effect of the porosity. Tribol. Int. **116**, 264–271 (2017). https://doi.org/10.1016/j.triboint.2017.07.022
40. Maegawa, S., Itoigawa, F., Nakamura, T.: A role of friction-induced torque in sliding friction of rubber materials. Tribol. Int. **93**, 182–189 (2016). https://doi.org/10.1016/j.triboint.2015.08.030
41. Scheibert, J., Dysthe, D.K.: Role of friction-induced torque in stick-slip motion. EPL. **92**(5), 620–622 (2010). https://doi.org/10.1209/0295-5075/92/54001
42. Mcadams, S.D., Tsui, T.Y., Oliver, W.C., Pharr, G.M.: Effects of interlayers on the scratch adhesion performance of ultrathin films of copper and gold on silicon substrates. MRS Online Proc. Libr. Arch. (1994). https://doi.org/10.1557/PROC-356-809
43. Scharf, T.W., Barnard, J.A.: Nanotribology of ultrathin a: SiC/SiC-N overcoats using a depth sensing nanoindentation multiple sliding technique. Thin Solid Films. **308**(1), 340–344 (1997). https://doi.org/10.1016/S0040-6090(97)00568-3
44. Li, K.J., Ni, B.Y.H., Li, J.C.M.: Stick-slip in the scratching of styrene-acrylonitrile copolymer. J. Mater. Res. **11**(6), 1574–1580 (1996). https://doi.org/10.1557/Jmr.1996.0197
45. Gao, C.H., Liu, M.: Characterization of spherical indenter with fused silica under small deformation by Hertzian relation and Oliver and Pharr's method. Vacuum. **153**, 82–90 (2018). https://doi.org/10.1016/j.vacuum.2018.03.061
46. Field, J.S., Swain, M.V.: A simple predictive model for spherical indentation. J. Mater. Res. **8**(2), 297–306 (1993). https://doi.org/10.1557/Jmr.1993.0297

47. Gao, C.H., Yao, L.G., Liu, M.: Berkovich nanoindentation of borosilicate K9 glass. Opt. Eng. 57(3) (2018). https://doi.org/10.1117/1.Oe.57.3.034104
48. Zhao, G.F., Liu, M., An, Z.N., Ren, Y., Liaw, P.K., Yang, F.Q.: Electromechanical responses of Cu strips. J. Appl. Phys. 113(18) (2013). https://doi.org/10.1063/1.4804938
49. Beake, B.D., Liskiewicz, T.W., Smith, J.F.: Deformation of Si(100) in spherical contacts—comparison of nano-fretting and nano-scratch tests with nano-indentation. Surf. Coat. Technol. **206**(7), 1921–1926 (2011)
50. Belak, J.: Nanotribology: modeling atoms when surfaces collide-energy and technology review. Energy Technol. Rev. (1994)
51. Bowden, F.P., Tabor, D.: The friction and lubrication of solids. Clarendon, Oxford (1950)
52. Carreon, A.H., Funkenbusch, P.D.: Material specific nanoscratch ploughing friction coefficient. Tribol. Int. **126**, 363–375 (2018). https://doi.org/10.1016/j.triboint.2018.05.027
53. Benjamin, P., Weaver, C.: Measurement of Adhesion of thin films. Proc. Royal Soc. Lond. **254**(1277), 163–176 (1960)
54. Laugier, M.T.: An energy approach to the adhesion of coatings using the scratch test. Thin Solid Films. **117**(4), 243–249 (1984). https://doi.org/10.1016/0040-6090(84)90354-7
55. Laugier, M.T.: Adhesion of Tic and Tin coatings prepared by chemical vapor-deposition on Wc-Co-based cemented carbides. J. Mater. Sci. **21**(7), 2269–2272 (1986). https://doi.org/10.1007/Bf01114266
56. Beegan, D., Chowdhury, S., Laugier, M.T.: A nanoindentation study of copper films on oxidised silicon substrates. Surf. Coat. Technol. **176**(1), 124–130 (2003). https://doi.org/10.1016/S0257-8972(03)00774-6
57. Liu, M.: Finite element analysis of large contact deformation of an elastic–plastic sinusoidal asperity and a rigid flat. Int. J. Solids Struct. **51**(21–22), 3642–3652 (2014). https://doi.org/10.1016/j.ijsolstr.2014.06.026
58. Liu, M., Proudhon, H.: Finite element analysis of contact deformation regimes of an elastic-power plastic hardening sinusoidal asperity. Mech. Mater. **103**, 78–86 (2016). https://doi.org/10.1016/j.mechmat.2016.08.015
59. Zok, F.W., Miserez, A.: Property maps for abrasion resistance of materials. Acta Mater. **55**(18), 6365–6371 (2007). https://doi.org/10.1016/j.actamat.2007.07.042
60. Shih, M.H., Yu, C.Y., Kao, P.W., Chang, C.P.: Microstructure and flow stress of copper deformed to large plastic strains. Scripta Mater. **45**(7), 793–799 (2001)
61. Barenblatt, G.I.: The mathematical theory of equilibrium cracks in brittle fracture. Adv. Appl. Mech. **7**, 55–129 (1962)
62. Akono, A.T., Reis, P.M., Ulm, F.J.: Scratching as a fracture process: from butter to steel. Phys. Rev. Lett. **106**(20), 204302 (2011). https://doi.org/10.1103/PhysRevLett.106.204302
63. Akono, A.T., Ulm, F.J.: Fracture scaling relations for scratch tests of axisymmetric shape. J. Mech. Phys. Solids. **60**(3), 379–390 (2012). https://doi.org/10.1016/j.jmps.2011.12.009
64. Akono, A.T., Ulm, F.J.: Scratch test model for the determination of fracture toughness. Eng. Fract. Mech. **78**(2), 334–342 (2011). https://doi.org/10.1016/j.engfracmech.2010.09.017
65. Singh, A., Tang, L., Dao, M., Lu, L., Suresh, S.: Fracture toughness and fatigue crack growth characteristics of nanotwinned copper. Acta Mater. **59**(6), 2437–2446 (2011). https://doi.org/10.1016/j.actamat.2010.12.043